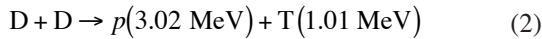
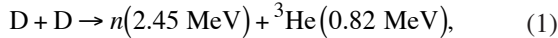


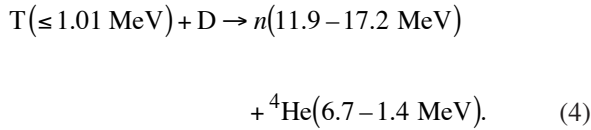
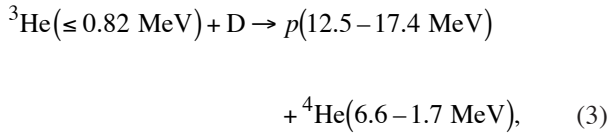
# Using Nuclear Data and Monte Carlo Techniques to Study Areal Density and Mix in D<sub>2</sub> Implosions

## Introduction

Maximizing the hot-fuel areal density ( $\rho R_{\text{hot}}$ ) and understanding the effects of mix upon it are fundamental issues of inertial confinement fusion (ICF).<sup>1–3</sup> One method used to estimate  $\rho R_{\text{hot}}$  of D<sub>2</sub>-filled capsule implosions is to measure the yields of secondary protons ( $Y_{2p}$ ) and/or secondary neutrons ( $Y_{2n}$ ) relative to the primary neutron yield ( $Y_{1n}$ ).<sup>4–12</sup> These secondary particles result from sequential reactions in which the energetic primary products of reactions



undergo fusion reactions with thermal deuterons in the fuel:



These processes produce secondary particles with spectra spread over significant energy intervals due to the kinetic energy of the primary reactants. The secondary-particle yields are typically two to three orders of magnitude lower than the primary yield, and the ratios  $Y_{2n}/Y_{1n}$  and  $Y_{2p}/Y_{1n}$  (which are linearly dependent on  $\rho R_{\text{hot}}$  in certain plasma regimes) can each be used to infer a value of  $\rho R_{\text{hot}}$  for implosions of D<sub>2</sub>-filled capsules in both direct- and indirect-drive experiments.<sup>12–15</sup> In those studies, the simple “hot-spot” and/or the “uniform” models were used to relate these ratios to  $\rho R_{\text{hot}}$ .

Although these simple models have been widely used to infer a value of  $\rho R_{\text{hot}}$ , they have some serious limitations that can result in misinterpretation and errors (as described in the next section); one manifestation of these problems is often disagreement between the proton- and neutron-inferred values of  $\rho R_{\text{hot}}$  calculated from experimental data (see Fig. 98.51). These deviations are related to a combination of mix, temperature profile, and the difference between the cross section for secondary reactions (3) and (4). These factors can cause secondary protons and neutrons to be produced in different regions of the compressed capsules (Fig. 98.52). In addition,

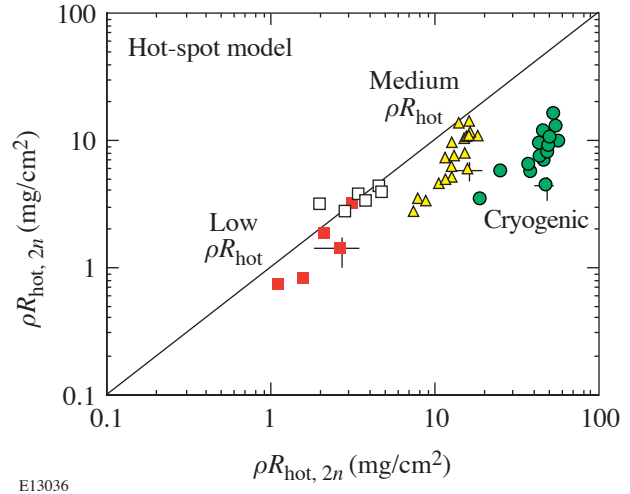
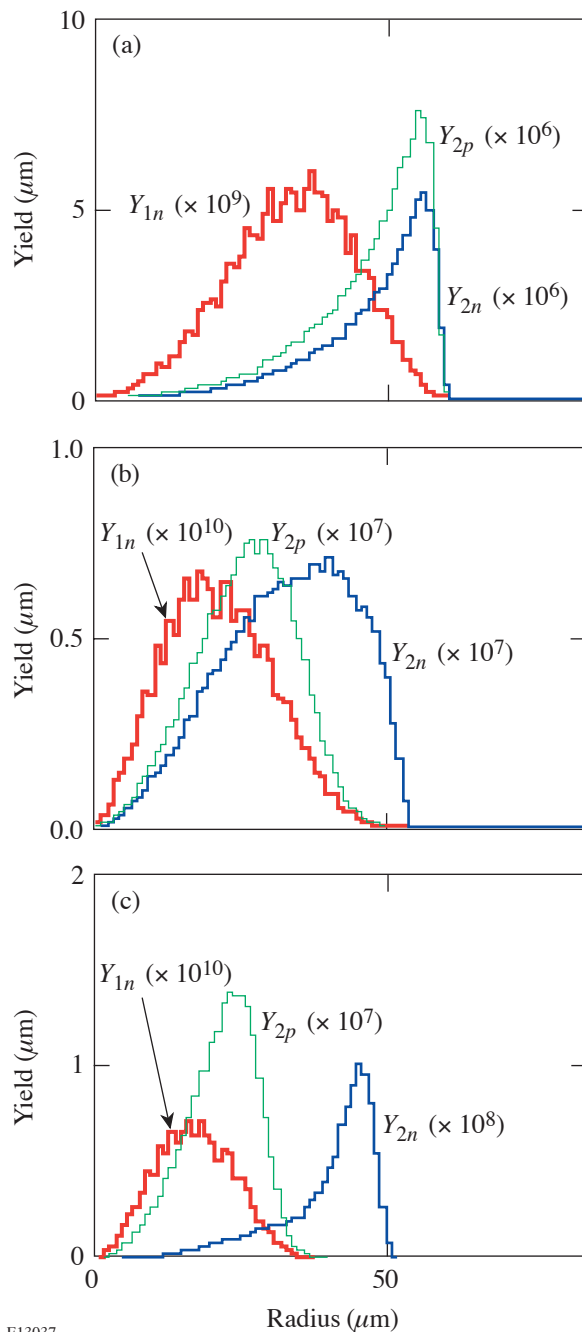


Figure 98.51

Secondary-proton- and secondary-neutron-implied values of  $\rho R_{\text{hot}}$  are compared for implosions of low  $\rho R_{\text{hot}}$  (squares), medium  $\rho R_{\text{hot}}$  (triangles), and cryogenic (circles) capsules on OMEGA. For low- $\rho R_{\text{hot}}$  implosions, the values of  $\rho R_{\text{hot}}$  inferred from secondary protons and neutrons using the simple hot-spot model agree well. It is also shown that values of  $\rho R_{\text{hot}}$  are larger for implosions with ~12-kJ laser energy (open squares) than for implosions with ~23-kJ laser energy (closed squares). For these dramatically overdriven implosions, it is possible that the effects of mix are coming back into play, as indicated by the observation that  $\rho R_{\text{hot},2n}$  is larger than  $\rho R_{\text{hot},2p}$ . For implosions with larger  $\rho R_{\text{hot}}$ , however, the values inferred from secondary neutrons are always larger than the values from secondary protons. The error bars shown are typical of each type of implosion; they include uncertainties in the measurements and in the assumed values of the density.



E13037

Figure 98.52  
 Calculated radial distributions of primary- and secondary-birth positions per unit length for (a) low- $\rho R$  implosion 30981, (b) medium- $\rho R$  implosion 27443, and (c) cryogenic implosion 28900. For low- $\rho R$  implosions, where  $\rho R_{2p}$  and  $\rho R_{2n}$  agree reasonably well, birth positions of secondary protons and neutrons are virtually identical. For medium- $\rho R$  and cryogenic implosions, however, where  $\rho R_{2n}$  is always larger than  $\rho R_{2p}$ , secondary neutrons are produced in more outer regions compared to secondary protons. Note that calculated radial distributions of primary birth rates per unit volume (as opposed to unit radius) are shown in Figs. 98.60–98.62 for these three implosions.

others have noted some puzzling issues with recent secondary-neutron measurements in indirect-drive implosions on OMEGA.<sup>16</sup> In that work, the authors observed a factor-of-3-larger  $Y_{2n}/Y_{1n}$  ratio and a narrower secondary-neutron spectrum than predicted for these low-convergence implosions (where mix should be relatively unimportant). In contrast, for high-convergence implosions, they found better agreement between measured and predicted  $Y_{2n}/Y_{1n}$  values.

In previous work,<sup>12</sup> high-resolution secondary-proton spectra were obtained during experiments on OMEGA.<sup>17</sup> The yields were used with measured neutron yields to estimate  $\rho R_{\text{hot}}$  with the hot-spot and uniform models, and it was shown that the  $Y_{2p}/Y_{1n}$ -inferred  $\rho R_{\text{hot}}$  was often lower than the  $Y_{2n}/Y_{1n}$ -inferred  $\rho R_{\text{hot}}$ . This was attributed to the effects of fuel-shell mix, and it was suggested that the two inferences might be considered lower and upper limits, respectively. In this article, that work is extended to cover a wider range of implosion types and to include Monte Carlo simulations that allow a detailed study of the implications of more-realistic models of the compressed core on the secondary production. The following sections (1) describe the hot-spot and uniform models and their limitations, (2) describe the experiments and the range of measured parameters, (3) describe a Monte Carlo program that will model the implosions to understand how particle production occurs, (4) discuss results from both experiments and Monte Carlo calculations, with an emphasis on how  $\rho R_{\text{hot}}$  is related to the yields of primary and secondary particles, and (5) summarize the results.

### Primary and Secondary Products

The hot-spot and uniform models have been commonly used to relate  $Y_{2p}/Y_{1n}$  and  $Y_{2n}/Y_{1n}$  to  $\rho R_{\text{hot}}$ . The hot-spot model assumes that an imploded capsule is a sphere of uniform density and temperature and that all primary reactions occur at the very center of the capsule. A fraction of the primary  ${}^3\text{He}$  (tritons) fuse with thermal deuterons, producing secondary protons (neutrons) as they move radially outward. As the primary particles travel through the D plasma, they lose energy, and the probability for producing secondary particles along the path varies greatly since the secondary  $D^3\text{He}$  and DT fusion cross sections ( $\sigma_{D^3\text{He}}$  and  $\sigma_{DT}$ ) are strong functions of the primary  ${}^3\text{He}$  and T energies [Fig. 98.53(a)].<sup>18</sup>  $\sigma_{D^3\text{He}}$  peaks at  $\sim 0.65$  MeV, close to the  ${}^3\text{He}$  birth energy (0.8 MeV), while  $\sigma_{DT}$  peaks at  $\sim 0.18$  MeV, significantly lower than the triton birth energy (1.0 MeV). As a result, secondary protons are mainly produced near the  ${}^3\text{He}$  birth position, while secondary neutrons are mainly produced farther away from the triton birth position [see Fig. 98.53(b)]. This information is used to calcu-

late  $\rho R_{\text{hot}}$  from  $Y_{2p}/Y_{1n}$  and  $Y_{2n}/Y_{1n}$ , and the resulting dependencies are shown in Fig. 98.54 for D plasmas with different temperatures and densities. The ratios each saturate at different values of  $\rho R_{\text{hot}}$  for different temperatures and densities because the primary  ${}^3\text{He}$  and tritons generally have significantly different ranges in the plasma. If either particle stops before leaving the fuel, it will not sample the entire  $\rho R_{\text{hot}}$ , and the implied value of  $\rho R_{\text{hot}}$  underestimates the actual value.  $Y_{2p}/Y_{1n}$  does not depend on temperature until it starts to saturate, while  $Y_{2n}/Y_{1n}$  is sensitive to temperature well below the saturation level. Therefore, without a reasonable estimate of plasma temperature,  $Y_{2n}/Y_{1n}$  cannot be used to accurately infer  $\rho R_{\text{hot}}$ .

The uniform model assumes that the primary particles are produced uniformly in a sphere of constant density and temperature. The  $Y_{2p}/Y_{1n}$  and  $Y_{2n}/Y_{1n}$  dependencies show similar behavior to the hot-spot model. The primary difference is that values of  $\rho R_{\text{hot}}$  implied by the uniform model are always larger than values from the hot-spot model because the mean

path length of primary particles in the D plasma is shorter by 25% in the uniform model, when saturation has not occurred. The simulations described in the **Results** section (p. 128) indicate that the hot-spot model gives more-meaningful values of  $\rho R_{\text{hot}}$  than the uniform model; therefore, the hot-spot model will be used throughout the remainder of this article.

Both models have limitations that can introduce errors into the analysis of  $\rho R_{\text{hot}}$ . These include the saturation of  $Y_{2p}$  and  $Y_{2n}$  and the uncertainty introduced by the temperature dependence of  $Y_{2n}$ . The shapes of temperature and density profiles and the presence of fuel-shell mix<sup>20–22</sup> can have substantial impact on secondary-particle production. In reality, the temperature is highest and the density is lowest at the center of the implosion. As the temperature decreases and the density increases, the rate of energy loss of primary particles becomes larger. This typically causes a reduction of the secondary-proton production rate and an enhancement of the secondary-neutron production rate [see Fig. 98.53(a)]. Fuel-shell mix

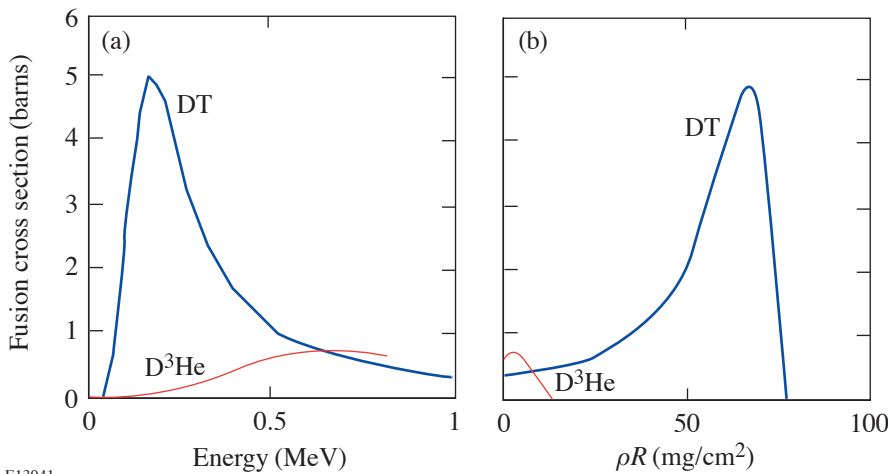


Figure 98.53

(a) Dependence of the secondary  $D^3\text{He}$  (DT) reaction cross section on the energy of the primary  ${}^3\text{He}$  (T) in a cold D plasma.<sup>18</sup> The  $D^3\text{He}$ -reaction cross section is peaked close to the birth energy of  ${}^3\text{He}$ , while the DT-reaction cross section peaks dramatically after T has lost most of its energy. (b) As a result, secondary protons are created close to the birth points of primary  ${}^3\text{He}$  (here defined as  $\rho R = 0$ ), while secondary neutrons are produced away from the birth points of primary T ( $\rho R = 0$ ). Although this plot is for a 1-g/cc, 3-keV D plasma, it looks similar for plasmas with different densities and temperatures.

E13041

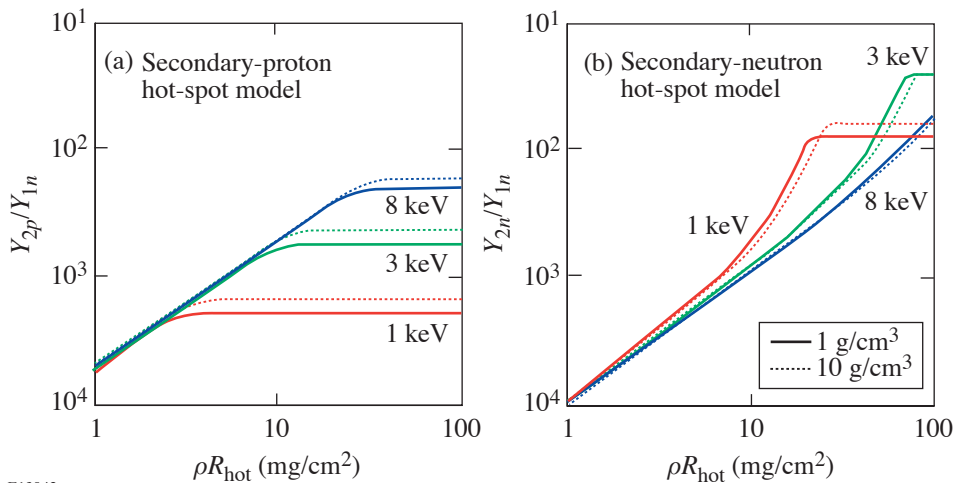


Figure 98.54

(a)  $Y_{2p}/Y_{1n}$  and (b)  $Y_{2n}/Y_{1n}$  as functions of  $\rho R_{\text{hot}}$  for a 1-, 3-, and 8-keV D plasma of 1 g/cc (solid line) and 10 g/cc (dotted line) using the hot-spot model. The energy losses of primary  ${}^3\text{He}$  and T were calculated according to Ref. 19, and the fusion cross sections were calculated according to Ref. 18.  $Y_{2p}/Y_{1n}$  is temperature independent until it reaches the saturation levels. In contrast,  $Y_{2n}/Y_{1n}$  is temperature dependent well below saturation levels.

E13042

lowers the temperature in the mix region, which increases the energy loss rate and results in a further reduction of the secondary-proton production rate and an enhancement of the secondary-neutron production rate. Shell material mixed into the fuel can directly affect secondary production by increasing the energy lost by T and  $^3\text{He}$  after traveling through a given amount of D, due to the higher effective charge of the shell material mixed in.

## Experiments

In the direct-drive experiments described here, distributed phase plates,<sup>23</sup> polarization smoothing using birefringent wedges,<sup>24</sup> and 1-THz, two-dimensional smoothing by spectral dispersion<sup>25</sup> were applied to smooth the OMEGA laser beams in order to enhance implosion uniformity and the nuclear reaction rate. Three types of capsules were used to study implosions with a wide range of areal densities: Low- $\rho R_{\text{hot}}$  implosions were studied using thin ( $\sim 3\text{-}\mu\text{m}$ ) glass ( $\text{SiO}_2$ ) shells filled with  $\sim 15$  atm of  $D_2$ . Some of these capsules were irradiated with a 1-ns square pulse delivering 23 kJ of on-target energy, while others were irradiated with a shorter (600- to 800-ps) pulse with on-target energy of  $\sim 12$  kJ.<sup>26</sup> Medium- and large- $\rho R$  implosions were studied using capsules with thick ( $\sim 20\text{-}\mu\text{m}$ ) plastic (CH) shells filled with  $\sim 15$  atm of  $D_2$  and cryogenic capsules with an  $\sim 100\text{-}\mu\text{m}$  layer of  $D_2$  ice enclosed within a 3- to  $\sim 5\text{-}\mu\text{m}$ -thick CH shell, respectively. They were all irradiated with 1-ns square pulses, delivering 23 kJ of on-target energy.

Charged-particle data were collected with two types of spectrometers: Wedged-range-filter proton spectrometers<sup>12,27</sup> provided secondary-proton spectra from up to six different directions simultaneously. These spectra were used to calculate the yield and mean energy of secondary protons. Two magnet-based charged-particle spectrometers<sup>27</sup> provided the spectra of primary protons and tritons for low- $\rho R$  implosions. Neutron data were obtained from three diagnostics: Neutron time-of-flight detectors<sup>28</sup> provided primary- and secondary-neutron yields as well as primary-neutron-yield-averaged ion temperature ( $\langle T_i \rangle_{Y_{1n}}$ ), and a neutron temporal diagnostic<sup>29</sup> measured the peak primary-neutron production time and the DD burn duration. In addition, secondary-neutron spectra were obtained from the 1020-scintillator array<sup>30</sup> on some of the more-recent implosions.

The data from each implosion then include the five quantities  $Y_{1n}$ ,  $Y_{2n}$ ,  $Y_{2p}$ ,  $\langle T_i \rangle_{Y_{1n}}$ , and  $\langle E_{2p} \rangle$ , which will be matched to simulations in the next section. In addition, the spectral energy distributions of the secondary protons (and sometimes second-

ary neutrons) will be compared with the simulations. The yields and  $\langle T_i \rangle_{Y_{1n}}$ , together with a realistic plasma density, can also be used to determine what the simple hot-spot and uniform models imply for values of  $\rho R_{\text{hot},2p}^{\text{expl}}$  and  $\rho R_{\text{hot},2n}^{\text{expl}}$  (where the superscript “expl” refers to the use of the measured  $\langle T_i \rangle_{Y_{1n}}$  as the characteristic ion temperature).

## Monte Carlo Simulations

A Monte Carlo program was developed to model the experiments described in the previous section. This allows us to use more-realistic temperature and density profiles than those in the hot-spot and uniform models. The burn-averaged ion temperature profile  $[T_i(r)]$  and the shell (or cold fuel, for cryogenic capsules) density profile  $[\rho_{\text{cold}}(r)]$  are assumed to have super- or sub-Gaussian profiles, and the six input parameters are  $T_{i0}$ ,  $T_{iw}$ ,  $T_{ip}$ ,  $S_{r0}$ ,  $S_w$ , and  $S_p$  characterizing the temperature and density profiles

$$T_i(r) = T_{i0} \exp\left[-(r/T_{iw})^{T_{ip}}\right] \quad (5)$$

and

$$\rho_{\text{cold}}(r) = \rho_{\text{cold}0} \exp\left\{-\left[(r - S_{r0})/S_w\right]^{S_p}\right\}. \quad (6)$$

These parameters are varied to produce simulated particle production that best fits the measured data for each implosion. The hot-fuel density profile  $[\rho_{\text{hot}}(r)]$  is calculated assuming that the plasma is isobaric out to the peak shell pressure region; with this constraint,  $\rho_{\text{cold}0}$  is then adjusted to conserve the fuel mass. (The initial fuel mass is calculated based on the initial fuel pressure and the size of the capsule.)

For computational purposes, each primary particle is assumed to produce a secondary particle, and a spectrum of particles per unit energy  $dN_2/dE$  is obtained. Since only a small fraction of the primary particles actually undergo secondary reactions, the secondary yield and spectrum need to be normalized according to  $Y_2 = \langle P_2 \rangle Y_1$  and

$$\begin{aligned} dY_2/dE &\approx \langle P_2 \rangle Y_1 (dN_2/dE)/N_2; \\ \langle P_2 \rangle &\equiv \left\langle \int n_D(l) \sigma_{\text{sec}}(l) dl \right\rangle \end{aligned}$$

is the probability of primary-to-secondary conversion, calculated in the program as the primary-yield-weighted mean value of the line integral of the D number density ( $n_D$ ) times the secondary fusion cross section ( $\sigma_{\text{sec}}$ ) for all possible primary-particle trajectories. The primary-particle production is determined by the density and temperature profiles. The particles are followed along their trajectories through the capsule until

they either escape or lose all of their energy. The energy loss is calculated, as briefly described in the next paragraph, in order to obtain  $\sigma_{\text{sec}}$  along paths of primary particles. The probability of a secondary fusion reaction is calculated along the path of the primary particle; then the birth position, direction, and energy of the secondary particle are calculated. The radial distributions of the primary- and secondary-particle birth positions are recorded as well to illustrate the effects of profiles and fuel-shell mix.

The energy loss of charged particles in plasmas is strongly dependent upon the velocity of the particle. Depending on the relative magnitude of the particle velocity  $v_p$  and the thermal velocity  $v_{\text{th}}$  of the background electrons, the plasma can be described as “cold” ( $v_p \gg v_{\text{th}}$ ), “warm” ( $v_p \sim v_{\text{th}}$ ), or “hot” ( $v_p \ll v_{\text{th}}$ ). The theory described in Ref. 19 predicts that the plasma-stopping power reaches a maximum when  $v_p \approx v_{\text{th}}$ , which was also demonstrated for the first time in Ref. 39. The general form for the charged-particle energy loss per unit distance,  $dE/dx$ , in fully ionized plasmas is given by<sup>19</sup>

$$-\frac{1}{Z^2} \frac{dE}{dX} = \left( \frac{\omega_p e}{v_p} \right)^2 G \left( \frac{v_p^2}{v_{\text{th}}^2} \right) \ln \Lambda, \quad (7)$$

where  $\omega_p = (4\pi n_e e^2 / m_e)^{1/2}$  is the electron-plasma frequency,  $Z$  is the projectile charge number,  $v_p$  is the velocity of the particle,  $v_{\text{th}} = (2T/m_e)^{1/2}$  is the thermal velocity of the plasma electrons, and  $\ln \Lambda$  is the Coulomb logarithm;  $n_e$ ,  $e$ , and  $m_e$  are the electron density, charge, and mass, respectively.  $G(v_p/v_{\text{th}})$  is the Chandrasekhar function, which peaks at  $v_p/v_{\text{th}} \approx 1$ , and explains why the stopping power reaches a maximum when  $v_p \approx v_{\text{th}}$ . The formulation given above applies to both plasma-electron stopping and plasma-ion stopping, where the latter, for the conditions of interest here, is about 10% of the stopping by electrons.

Since the model is static, the primary yield is calculated by multiplying the burn profile by the burn duration (full width at half maximum of the neutron-production rate); therefore, the error in the measurement of the burn duration is included in the error of the primary yield.  $\langle E_{2p} \rangle$  is calculated from the secondary-proton spectrum, and  $\langle T_i \rangle_{Y_{1n}}$  is determined in the region where the primary particles are produced.<sup>31</sup> Each of the six input parameters is varied over a large range, initially using large steps to identify the region of small  $\chi^2$ . This region is then more carefully explored using finer grids; as a result, the six-dimensional parameter space is explored completely. For each set of model parameters, the predicted values of the experi-

mentally measured quantities are calculated and the quality of agreement with the data from a particular implosion is characterized with the total  $\chi^2$ , which takes into account uncertainties in the experimental measurements. For each implosion, it is found that multiple local minima exist within the space of model parameters but there is one clear region with the smallest values of  $\chi^2$ . Errors in the values of individual model parameters are then estimated by asking how much they can be changed without causing the total  $\chi^2$  to increase by more than 1. Although the widths and shapes of secondary-proton spectra are not used as fit criteria, it will be seen that the predicted spectra match the measured spectra quite well; this fact provides extra confidence that the best-fit-model parameters are realistic.

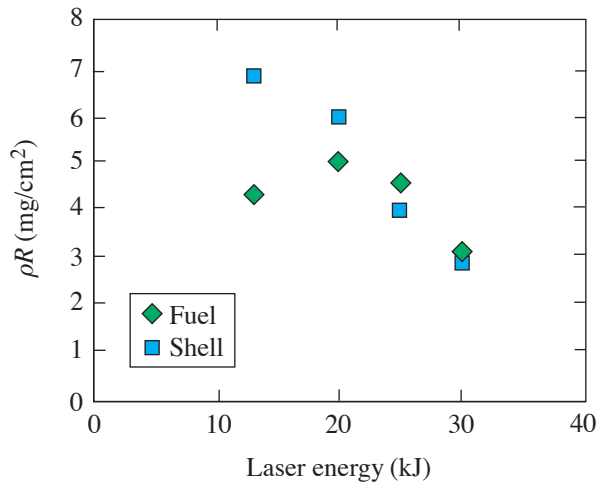
The characteristics of the best-fit model for each implosion were used to determine how realistic the hot-spot-model inferred values of  $\rho R_{\text{hot}}$  are. Values of  $Y_{2p}/Y_{1n}$ ,  $Y_{2n}/Y_{1n}$ ,  $\langle T_i \rangle_{Y_{1n}}$ , and plasma density from the simulations were used to infer  $\rho R_{\text{hot},2p}^{\text{sim1}}$  and  $\rho R_{\text{hot},2n}^{\text{sim1}}$  according to Fig. 98.54 (the superscript “sim1” indicates that  $\langle T_i \rangle_{Y_{1n}}$  was used as the characteristic ion temperature). The values of  $\rho R_{\text{hot},2p}^{\text{sim2}}$  and  $\rho R_{\text{hot},2n}^{\text{sim2}}$  were calculated assuming that the appropriate temperatures are averages weighted by secondary yields  $\langle T_i \rangle_{Y_{2p}}$  and  $\langle T_i \rangle_{Y_{2n}}$ , respectively. These values were then compared with  $\rho R_{\text{hot}}^{\text{int}} \equiv \int \rho_D dr$ , integrated over the hot-fuel region.

## Results

### 1. Low-Areal-Density Implosions

For low- $\rho R_{\text{hot}}$  implosions, the primary <sup>3</sup>He and T traverse the entire hot-fuel region, and the values of  $\rho R_{\text{hot}}$  inferred from secondary protons and neutrons using the hot-spot (or uniform) model generally agree with each other and usually give a reasonable estimate of the actual value of  $\rho R_{\text{hot}}$ . This is shown experimentally by the square points in Fig. 98.51, which compares values of  $\rho R_{\text{hot},2p}^{\text{expl}}$  and  $\rho R_{\text{hot},2n}^{\text{expl}}$ . These values were inferred according to Fig. 98.54 assuming a D plasma with a temperature of  $\langle T_i \rangle_{Y_{1n}}$  keV and a density of 1.5 g/cc (obtained from a typical best-fit simulation, as discussed below). Figure 98.51 also illustrates that  $\rho R_{\text{hot},2p}^{\text{expl}}$  and  $\rho R_{\text{hot},2n}^{\text{expl}}$  are larger for implosions with lower (~12 kJ) on-target laser energy (open squares) than for implosions with full (~23 kJ) laser energy (closed squares). This could be explained by a larger amount of glass shell being ablated away in full-energy implosions, resulting in less material to drive the fuel inward<sup>32,33</sup> (Fig. 98.55). In addition, these values of  $\rho R_{\text{hot}}^{\text{expl}}$  from D<sub>2</sub> implosions with full laser energy show reasonable agreement with values from similar thin-glass-shell DT

implosions,<sup>34,12</sup> for which the knock-on method<sup>35</sup> was used to determine the  $\rho R_{\text{hot}}$ .



E13043

Figure 98.55

One-dimensional clean *LILAC* simulations for low- $\rho R$  implosion 30981 indicate that hot-fuel  $\rho R$  starts to decrease as the capsule is significantly overdriven. This trend agrees with measurements where  $\rho R_{\text{hot}}$  is lower for full-laser-energy-driven (~23-kJ), thin-glass-shell capsules than for low-laser-energy-driven (~12-kJ) capsules (Fig. 98.51).

For implosion 30981, which involved a 3.1- $\mu\text{m}$  glass shell filled with 14.7 atm of  $D_2$  gas, Fig. 98.56(a) shows simulated density and temperature profiles from the best-fit simulation. Figure 98.56(b) shows radial distributions of the primary- and secondary-particle-birth positions; secondary protons and neutrons are produced in virtually identical regions of the capsule. In addition, a high plasma temperature and a low  $\rho R_{\text{hot}}$  result in similar values of  $\rho R_{\text{hot}}^{\text{sim1}}$  inferred from the simulated secondary yields. Values of  $\rho R_{\text{hot}}^{\text{sim1}}$  are inferred using the hot-spot model and assuming a plasma temperature of  $\langle T_i \rangle_{Y_{1n}}$  keV and a plasma density of 1.5 g/cc (obtained from simulation). In addition, values of  $\rho R_{\text{hot}}^{\text{sim1}}$  agree with  $\rho R_{\text{hot}}^{\text{int}}$  obtained from the fuel-density profile shown in Fig. 98.56(a); this indicates that the small amount of fuel-shell mix in this type of implosion does not have much impact on the accuracy of the simple model. Results of the simulation along with measured data are summarized in Table 98.IV.

Simulated secondary spectra are in good agreement with measured spectra as shown in Figs. 98.56(c) and 98.56(d). The measured secondary-proton spectrum is an average of five spectra obtained simultaneously at different angles from implosion 30981.

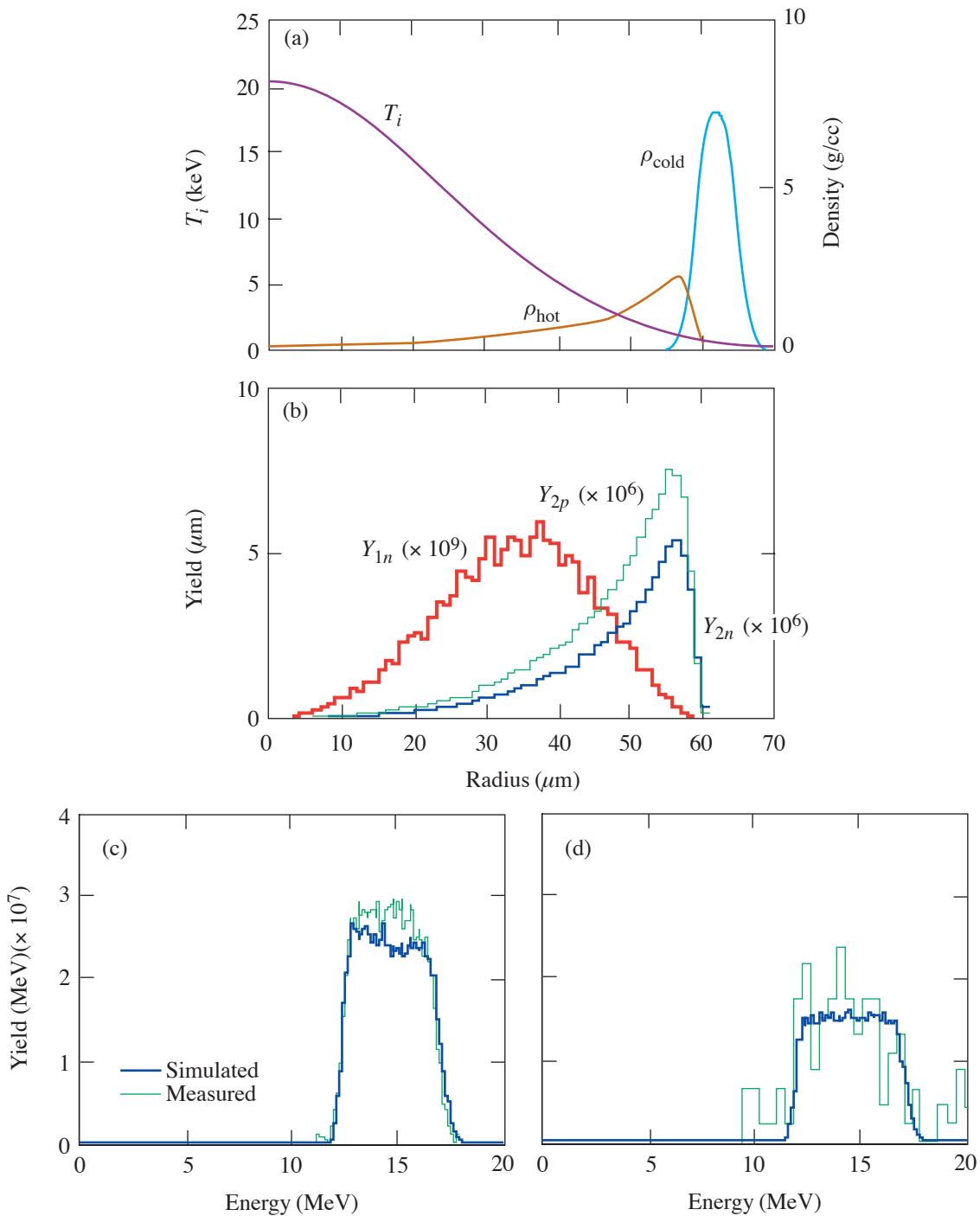
## 2. Medium-Areal-Density Implosions

Correctly inferring the value of  $\rho R_{\text{hot}}$  is more difficult for implosions of capsules with thick plastic shells because  $Y_{2p}$  reaches saturation when  $\rho R_{\text{hot}}$  is sufficiently large, and  $Y_{2n}$  is enhanced in the presence of increased fuel-shell mix. The triangles in Fig. 98.51 show that the values of  $\rho R_{\text{hot},2p}^{\text{exp1}}$  are often smaller than the values of  $\rho R_{\text{hot},2n}^{\text{exp1}}$ , as previously reported in Ref. 12. Values of  $\rho R_{\text{hot},2p}^{\text{exp1}}$  and  $\rho R_{\text{hot},2n}^{\text{exp1}}$  are inferred assuming a temperature of  $\langle T_i \rangle_{Y_{1n}}$  keV and a D plasma with a density of 2 g/cc.

Figure 98.57(a) shows the temperature and density profiles that result in the best fit to the measured data for implosion 27443 (19.4- $\mu\text{m}$  plastic shell filled with 15 atm of  $D_2$  gas), and Fig. 98.57(b) shows the resulting radial distributions of primary- and secondary-particle-birth positions. About 32% of the initial CH mass remains, and ~1.3  $\mu\text{m}$  of the initial CH layer has mixed into the fuel (which is similar to the amount of mix reported in Refs. 20–22).<sup>36</sup> The  $^3\text{He}$  are ranged out before traversing the entire fuel region. Figure 98.57(b) also illustrates an enhancement of  $Y_{2n}$  by fuel-shell mix; the increased energy loss of T per unit  $\rho R_{\text{hot}}$ , due to the cooler, dense shell material, results in an enhanced DT fusion cross section (Fig. 98.53), which causes  $Y_{2n}/Y_{1n}$  to overestimate  $\rho R_{\text{hot}}^{\text{int}}$ . In addition,  $Y_{2n}/Y_{1n}$  is more sensitive to temperature in this  $\rho R_{\text{hot}}$  range; using  $\langle T_i \rangle_{Y_{1n}}$ , which is always higher than  $\langle T_i \rangle_{Y_{2n}}$ , results in a larger inferred value of  $\rho R_{\text{hot}}$ .

Simulated yields and additional parameters characterizing the implosion are summarized and compared with measurements in Table 98.V. This table shows that the values of  $\rho R_{\text{hot}}^{\text{sim1}}$  implied by secondary protons and neutrons are smaller and larger than the value of  $\rho R_{\text{hot}}^{\text{int}}$ , respectively. The hot-spot model was used to obtain values of  $\rho R_{\text{hot}}$  using  $\langle T_i \rangle_{Y_{1n}}$  keV for the temperature and assuming the density of the D plasma was 2 g/cc.

The simulated secondary-proton spectrum is compared with the measured spectrum in Fig. 98.57(c). The measured secondary-proton spectrum is an average of three spectra simultaneously obtained at different angles from implosion 27443 and shows more downshift than spectra from the low- $\rho R_{\text{hot}}$  implosions. The widths of the secondary-proton and secondary-neutron spectra [Fig. 98.57(d)] are slightly narrower than in the previous case because the average energy of the primary particle, at the time it undergoes secondary fusion, is smaller.<sup>12</sup>



E13044

Figure 98.56

Parameters from the best-fit Monte Carlo simulation of shot 30981 (3.1- $\mu\text{m}$   $\text{SiO}_2$  shell filled with 14.7 atm of  $D_2$ ). (a)  $T_i(r)$  and  $\rho(R)$ . Fuel mass is fully conserved, while 11% of the shell mass remains. (b) Radial distributions of the birth positions of primary and secondary particles indicate that secondary protons and neutrons are produced in a virtually identical region of the capsule. (c) Measured and simulated secondary-proton and (d) secondary-neutron spectra. Note that the shape and width of the simulated proton spectrum are very similar to those of the measured spectrum, even though these were not part of the fitting procedure. The difference in simulated and measured secondary yields is within the measurement uncertainties. Measured and simulated values of implosion characteristics are summarized in Table 98.IV. Figure 98.60 indicates how the radial profiles of  $T_i$  and  $\rho$  can change without changing too much the quality of the fit to the data.

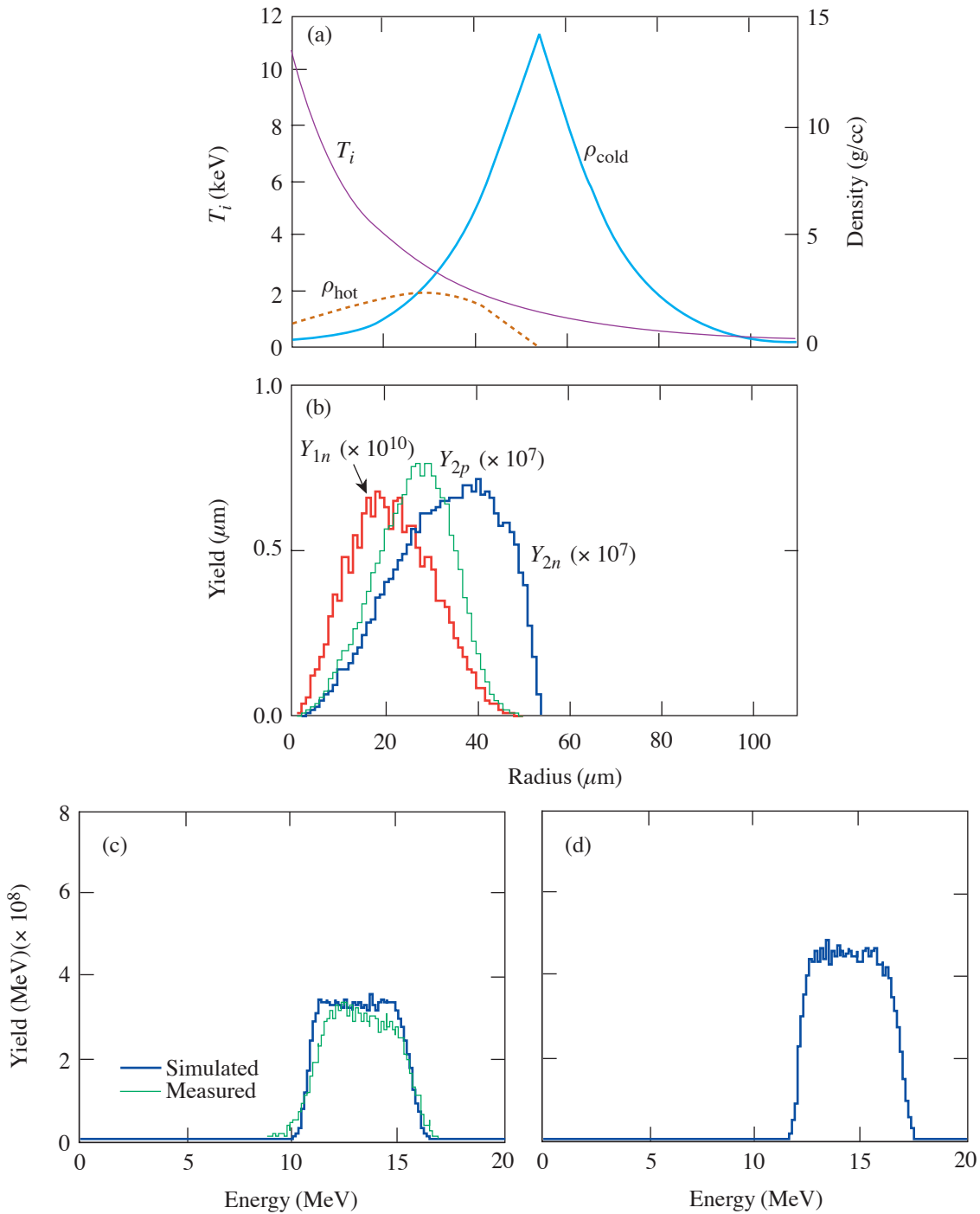
Table 98.IV: Measured and simulated values of yields and  $\rho R$  for OMEGA implosion 30981. Experimental data were fitted by adjusting  $\rho(R)$  and  $T_i(r)$ . Total  $\chi^2$  along with parameters specifying the cold (SiO<sub>2</sub>) temperature and density Gaussian profiles [peak temperature ( $T_{i0}$ ), 1/e radius ( $T_{iw}$ ), power of the exponent ( $T_{ip}$ ), peak density radius ( $S_{r0}$ ), 1/e radius ( $S_w$ ), and power of the exponent ( $S_p$ )] are also listed.  $\rho R_{\text{cold}} = \int \rho_{\text{cold}} dr$ , integrated radially over the SiO<sub>2</sub> shell region, and  $\rho R_{\text{hot}} = \int \rho_D dr$ , integrated radially over the hot-fuel region of the simulated profiles. Values of  $\rho R_{\text{hot},2n}$  and  $\rho R_{\text{hot},2p}$  were deduced using measured and simulated yield ratios assuming a  $1.5 \pm 1$ -g/cc [obtained from Fig. 98.56(a)] D plasma at  $\langle T_i \rangle_{Y_{1n}} \pm 0.5$  keV.

Shot 30981		
	Measured	Simulated
$Y_{1n}$	$(1.5 \pm 0.15) \times 10^{11}$	$(1.5 + 0.23 - 0.18) \times 10^{11}$
$Y_{2n}/Y_{1n}$	$(5.1 \pm 0.98) \times 10^{-4}$	$(5.1 + 1.1 - 0.57) \times 10^{-4}$
$Y_{2p}/Y_{1n}$	$(7.9 \pm 1.1) \times 10^{-4}$	$(7.6 + 1.0 - 0.96) \times 10^{-4}$
$\langle E_{2p} \rangle$ (MeV)	$14.47 \pm 0.1$	$14.64 + 0.14 - 0.16$
$\langle T_i \rangle_{Y_{1n}}$ (keV)	$8.2 \pm 0.5$	$8.2 + 0.7 - 0.5$
$\chi^2$	...	0.1
$T_{i0}$ (keV)	...	$20.5 + 2.5 - 10$
$T_{iw}$ ( $\mu\text{m}$ )	...	$34 + 14 - 4$
$T_{ip}$	...	$2 + 5 - 0$
$S_{r0}$ ( $\mu\text{m}$ )	...	$62 + 6 - 10$
$S_w$ ( $\mu\text{m}$ )	...	$3.5 + 3 - 3.3$
$S_p$	...	$2.5 + 7.5 - 2$
$\rho R_{\text{cold}}$ (mg/cm <sup>2</sup> )	...	$4.5 + 4.3 - 4.2$
$\rho R_{\text{hot}}$ (mg/cm <sup>2</sup> )	...	$3.7 + 0.8 - 0.4$
$\rho R_{\text{hot},2n}$ (mg/cm <sup>2</sup> )	$4.6 + 0.9 - 1.2$	$4.6 + 1.0 - 0.6$
$\rho R_{\text{hot},2p}$ (mg/cm <sup>2</sup> )	$4.3 + 0.6 - 0.8$	$4.1 \pm 0.5$

### 3. Cryogenic Implosions

For cryogenic implosions, the interpretation of inferred values of  $\rho R_{\text{hot}}$  is even more subtle since there is a high-temperature, low-density fuel region and a low-temperature, high-density fuel region. If most of the secondary particles are produced only in the hot-fuel region,  $Y_2/Y_{1n}$  can be used to infer  $\rho R_{\text{hot}}$ . On the other hand, if secondary particles are produced mainly in the inner part of the cold-fuel region, the inferred  $\rho R$  is larger than  $\rho R_{\text{hot}}$ , but smaller than  $\rho R_{\text{total}}$ . (Even

the more-penetrating T cannot traverse the entire cold-fuel region since the range of T in an 8-g/cc, 1-keV D plasma is  $\sim 15$  mg/cm<sup>2</sup>, and we usually calculate  $\rho R_{\text{total}} > 40$  mg/cm<sup>2</sup> from the downshift of the average secondary-proton energy for cryogenic implosions.) Figure 98.51 shows that values of  $\rho R_{\text{hot}}$  implied by measured  $Y_{2n}/Y_{1n}$  are always larger than values from measured  $Y_{2p}/Y_{1n}$  for those implosions (values were inferred assuming a  $\langle T_i \rangle_{Y_{1n}}$  keV, 3-g/cc D plasma).



E13045

Figure 98.57

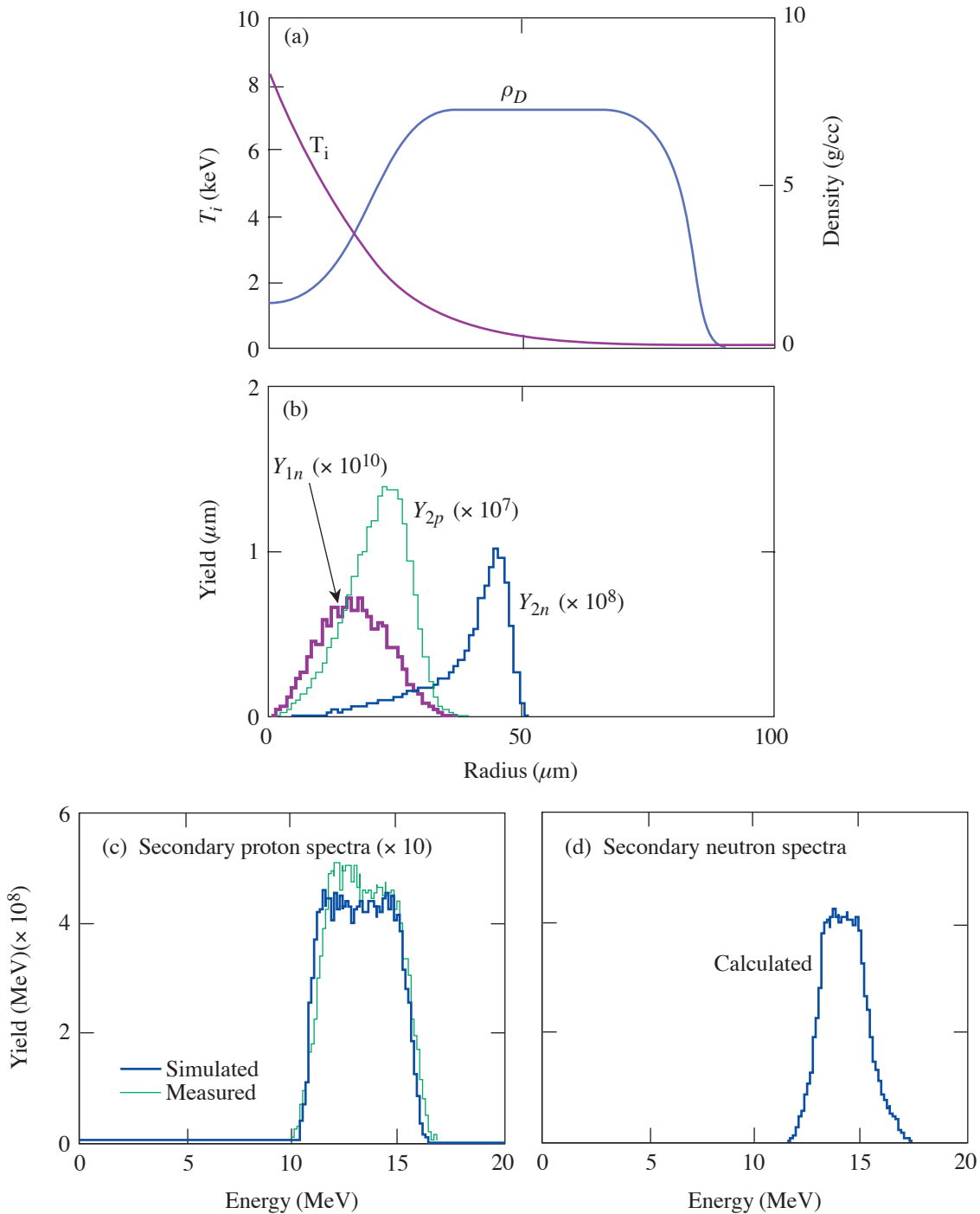
Best-fit parameters from the Monte Carlo simulation for shot 27443, which involved a  $19.4\text{-}\mu\text{m}$  CH shell filled with 15 atm of  $D_2$ . (a)  $T_i(r)$  and  $\rho(r)$ . Fuel mass is fully conserved, while 32% of the shell mass remains. (b) Radial distributions of the birth positions of primary and secondary particles show that secondary-proton production is diminished, while secondary-neutron production is enhanced in the region of significant fuel-shell mix. This causes secondary protons to underestimate and secondary neutrons to overestimate the actual value of  $\rho R_{\text{hot}}$ . (c) Measured and simulated secondary-proton spectra are compared, and (d) simulated secondary-neutron spectrum is shown. The secondary-proton spectra show more energy downshift, and the width of the secondary spectra are slightly narrower than the low  $\rho R_{\text{hot}}$  case because the average primary particle energy is smaller at the time of secondary reaction. Measured and simulated values of implosion characteristics are listed in Table 98.V, while other fits are illustrated in Fig. 98.61.

Table 98.V: Measured and simulated values of implosion characteristics for OMEGA implosion 27443. Values  $\rho R_{\text{hot}}$  were calculated assuming a  $2 \pm 1$ -g/cc D plasma at  $\langle T_i \rangle_{Y_{1n}} \pm 0.5$  keV. Results from simulation indicate that the  $\rho R_{\text{hot},2p}$  underestimates and  $\rho R_{\text{hot},2n}$  overestimates the actual value.

Shot 27443		
	Measured	Simulated
$Y_{1n}$	$(1.5 \pm 0.15) \times 10^{11}$	$(1.6 + 0.1 - 0.25) \times 10^{11}$
$Y_{2n}/Y_{1n}$	$(1.5 \pm 0.24) \times 10^{-3}$	$(1.4 + 0.16 - 0.12) \times 10^{-3}$
$Y_{2p}/Y_{1n}$	$(1.0 \pm 0.14) \times 10^{-3}$	$(1.0 + 0.1 - 0.15) \times 10^{-3}$
$\langle E_{2p} \rangle$ (MeV)	$13.1 \pm 0.1$	$13.07 + 0.1 - 0.11$
$\langle T_i \rangle_{Y_{1n}}$ (keV)	$4.1 \pm 0.5$	$4.1 + 0.2 - 0.4$
$\chi^2$	...	0.5
$T_{i0}$ (keV)	...	$11 + 0 - 5.5$
$T_{iw}$ ( $\mu\text{m}$ )	...	$20 + 18 - 0$
$T_{ip}$	...	$0.8 + 1.2 - 0$
$S_{r0}$ ( $\mu\text{m}$ )	...	$54 \pm 2$
$S_w$ ( $\mu\text{m}$ )	...	$16 + 2 - 6$
$S_p$	...	$1.2 + 0 - 0.2$
$\rho R_{\text{cold}}$ (mg/cm <sup>2</sup> )	...	$42.3 + 3.9 - 2.1$
$\rho R_{\text{hot}}$ (mg/cm <sup>2</sup> )	...	$8.9 + 1 - 0.4$
$\rho R_{\text{hot},2n}$ (mg/cm <sup>2</sup> )	$12.8 \pm 1.9$	$11.6 + 1.2 - 1$
$\rho R_{\text{hot},2p}$ (mg/cm <sup>2</sup> )	$5.0 \pm 0.7$	$5.2 + 0.5 - 0.7$

Radial profiles of temperature and density calculated for implosion 28900 (89- $\mu\text{m}$   $D_2$ -ice layer inside a 5.1- $\mu\text{m}$  CH shell) are shown in Fig. 98.58(a), and simulated and measured spectra are shown in Figs. 98.58(c) and 98.58(d). As indicated in Fig. 98.58(d) and Fig. 98.59, the secondary-neutron spectrum is much narrower than the secondary-neutron spectra from Figs. 98.56(d) and 98.57(d) because the primary T are, on average, less energetic when they fuse with thermal D.<sup>12</sup> Measurements of secondary-neutron spectra from more-recent cryogenic implosions also show the same characteristics.

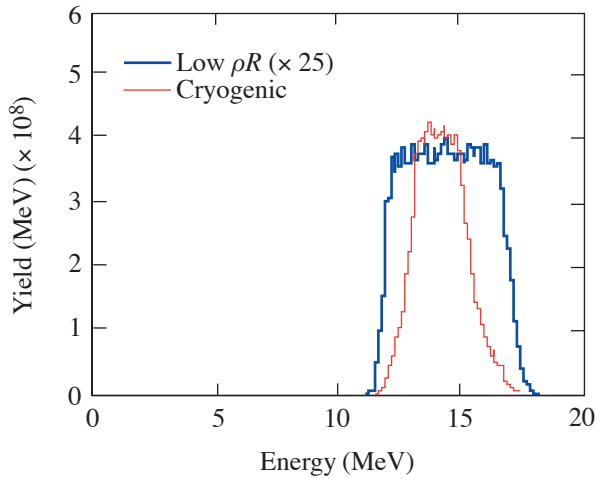
The radial distributions of the primary- and secondary-birth positions shown in Fig. 98.58(b) indicate that secondary protons and neutrons are born mainly in the hot- and cold-fuel regions, respectively. Therefore, the  $\rho R$  obtained from secondary protons gives an estimate of  $\rho R_{\text{hot}}$ , while the secondary-neutron yield provides a lower limit on  $\rho R_{\text{total}}$ . In this type of implosion, effects of mix or exchange of hot and cold fuel play significant roles in determining the radial distribution of secondary-birth positions.



E13046

Figure 98.58

(a) Simulated profile of shot 28900 (cryogenic capsule with a  $5.1\text{-}\mu\text{m}$  CD shell and  $89\text{-}\mu\text{m}$   $D_2$ -ice layer), which gives the best fit to the measurement; 31% of the total mass remains. (b) Radial distributions of the birth points of primary and secondary particles show that most of the secondary protons are produced in the hot-fuel region, while secondary neutrons are mainly produced in the cold-fuel region. (c) Measured and simulated secondary-proton spectra. (d) Simulated secondary neutron spectrum is narrower than the spectra in Figs. 98.56(d) and 98.57(d) because primary T are less energetic at the time they undergo secondary reactions;  $\rho R$  of cold fuel is large enough to stop primary T [Fig. 98.58(b)], and the cross section increases as T loses energy [Fig. 98.53(a)]. Important implosion characteristics are summarized in Table 98.VI, while other fits are illustrated in Fig. 98.62.



E13047

Simulated values of yields and other important implosion characteristics are compared with measured results in Table 98.VI. The secondary-neutron, hot-spot-model-inferred  $\rho R^{\text{sim1}}$  is close to  $\rho R^{\text{int}}_{\text{total}}$ , but this does not mean that the hot-spot model describes the implosion accurately. The agreement is an accidental consequence of using the wrong temperature  $\langle T_i \rangle_{Y_{1n}}$ , which samples the hotter central region rather than the cooler fuel region where most of the secondary neutrons are produced.

This implosion has also been analyzed using a combination of x-ray and neutron measurements, without the use of secondary-proton data. These results are discussed in Ref. 37. While the best-fit profiles were somewhat different, they agree within the uncertainties of the two simulation techniques.

## Conclusions

The hot-spot and uniform models have been used to infer the areal density of the hot-fuel region ( $\rho R_{\text{hot}}$ ) of  $D_2$  implosions, but disagreements between the values of  $\rho R_{\text{hot}}$  inferred from secondary-proton and secondary-neutron yields have often been observed, indicating limitations in these models. Results from direct-drive experiments on the OMEGA laser system and Monte Carlo simulations provided a deeper understanding of the relationship between  $\rho R$ , the capsule structure, and secondary-particle production. Experiments show that values of  $\rho R_{\text{hot}}$  inferred from the ratios of secondary-proton and neutron-to-primary neutron yields ( $Y_{2p}/Y_{1n}$  and  $Y_{2n}/Y_{1n}$ ) using the hot-spot model agree well for low- $\rho R_{\text{hot}}$  implosions (thin-glass-shell capsules), and simulations indicate that they

Figure 98.59

The simulated secondary-neutron spectrum is narrower than the spectra in Figs. 98.56(d) and 98.57(d) because the primary T are less energetic at the time they undergo secondary reactions;  $\rho R$  of cold fuel is large enough to stop primary T [Fig. 98.58(b)], and the cross section increases as T loses energy [Fig. 98.53(a)]. Note that detailed analysis of secondary-neutron spectra was used to study areal density in Ref. 10.

give a good estimate of the actual value of  $\rho R_{\text{hot}}$ . The results from implosions of  $D_2$ -filled, thin-glass shells also show reasonably good agreement with results from implosions of similar capsules filled with DT gas. For thick-plastic-shell-capsule implosions, where the  $\rho R_{\text{hot}}$  of an implosion becomes sufficiently large,  $Y_{2p}/Y_{1n}$  underestimates  $\rho R_{\text{hot}}$  since the primary  $^3\text{He}$  are ranged out before sampling the entire hot-fuel region. In addition, fuel-shell mix increases the rate of energy loss of  $^3\text{He}$  and causes  $Y_{2p}/Y_{1n}$  to further underestimate  $\rho R_{\text{hot}}$ . The fuel-shell mix also causes  $Y_{2n}/Y_{1n}$  to overestimate  $\rho R_{\text{hot}}$  by slowing down the primary T, thereby increasing the secondary DT fusion reaction cross section. As a result, values of  $\rho R_{\text{hot}}$  for medium  $\rho R_{\text{hot}}$  capsules inferred from  $Y_{2p}/Y_{1n}$  and  $Y_{2n}/Y_{1n}$  using the hot-spot model should be interpreted as estimates of the lower and upper limits on the actual  $\rho R_{\text{hot}}$ , respectively. For cryogenic capsules, secondary protons are produced mainly in the hot-fuel region, and the proton-implied value of  $\rho R$  provides a good estimate of the hot-fuel  $\rho R$ . In contrast, secondary neutrons are mostly produced in the inner part of the cold-fuel region, and the neutron-implied  $\rho R$  gives a lower limit on the total  $\rho R$  when calculated correctly using the average temperature and density of the secondary-neutron birth point. Naive use of the simple hot-spot or uniform model, with a burn-averaged temperature, often results in inaccurate inference of  $\rho R_{\text{hot}}$ . A more-thorough analysis, such as the use of complete data sets and simulations to determine the secondary-birth positions and the effects of mix, as presented herein, or the use of detailed analysis of secondary-neutron spectra both from experiments and simulations,<sup>10</sup> is required in order to obtain a realistic estimate of  $\rho R_{\text{hot}}$ .

Table 98.VI: Measured and simulated values of implosion characteristics for OMEGA implosion 28900.  $\rho R_{\text{total}} = \int \rho_D dr$ , integrated radially over the entire simulated profiles;  $\rho R_{\text{hot}}$  is defined as the  $\rho R$  that includes 90% of primary production. Values of  $\rho R_{\text{hot}}$  were calculated assuming a  $3.0 \pm 1.5$ -g/cc D plasma at  $\langle T_i \rangle_{Y_{1n}} \pm 0.5$  keV. Results from the simulation suggest that the value of  $\rho R_{\text{hot},2p}$  provides a good estimate of  $\rho R_{\text{hot}}$ . Secondary-neutron implied  $\rho R_{\text{hot}}$  is similar to  $\rho R_{\text{total}}$ , but this is because the value of the temperature used to infer  $\rho R_{\text{hot}}$  is too large. If the temperature of the cold-fuel region (1 keV instead of 3.6 keV) were used, a much smaller and physical value of  $\rho R_{\text{hot}}$  would be implied.

<b>Shot 28900</b>		
	<b>Measured</b>	<b>Simulated</b>
$Y_{1n}$	$(1.2 \pm 0.12) \times 10^{11}$	$(1.3 + 0.12 - 0.14) \times 10^{11}$
$Y_{2n}/Y_{1n}$	$(9.4 \pm 1.4) \times 10^{-3}$	$(9.1 + 1.0 - 1.1) \times 10^{-3}$
$Y_{2p}/Y_{1n}$	$(1.8 \pm 0.26) \times 10^{-3}$	$(1.6 + 0.0 - 0.2) \times 10^{-3}$
$\langle E_{2p} \rangle$ (MeV)	$13.31 \pm 0.10$	$13.28 + 0.5 - 0.11$
$\langle T_i \rangle_{Y_{1n}}$ (keV)	$3.6 \pm 0.5$	$3.5 + 0.6 - 0.3$
$\chi^2$	...	0.6
$T_{i0}$ (keV)	...	$8.5 + 9.5 - 2.5$
$T_{iw}$ ( $\mu\text{m}$ )	...	$18 + 10 - 8$
$T_{ip}$	...	$1.2 + 0.6 - 0.4$
$S_{r0}$ ( $\mu\text{m}$ )	...	$52 + 22 - 2$
$S_w$ ( $\mu\text{m}$ )	...	$32 + 16 - 12$
$S_p$	...	$9 + \geq 1 - 7.5$
$\rho R_{\text{total}}$ (mg/cm <sup>2</sup> )	...	$48.2 + 3.2 - 6.0$
$\rho R_{\text{hot}}$ (mg/cm <sup>2</sup> )	...	$7.9 + 0.2 - 1.7$
$\rho R_{\text{hot},2n}$ (mg/cm <sup>2</sup> )	$49.8 + 5.0 - 6.9$	$48.0 + 4.9 - 4.0$
$\rho R_{\text{hot},2p}$ (mg/cm <sup>2</sup> )	$9.3 + 1.9 - 1.5$	$7.8 + 0.5 - 0.6$

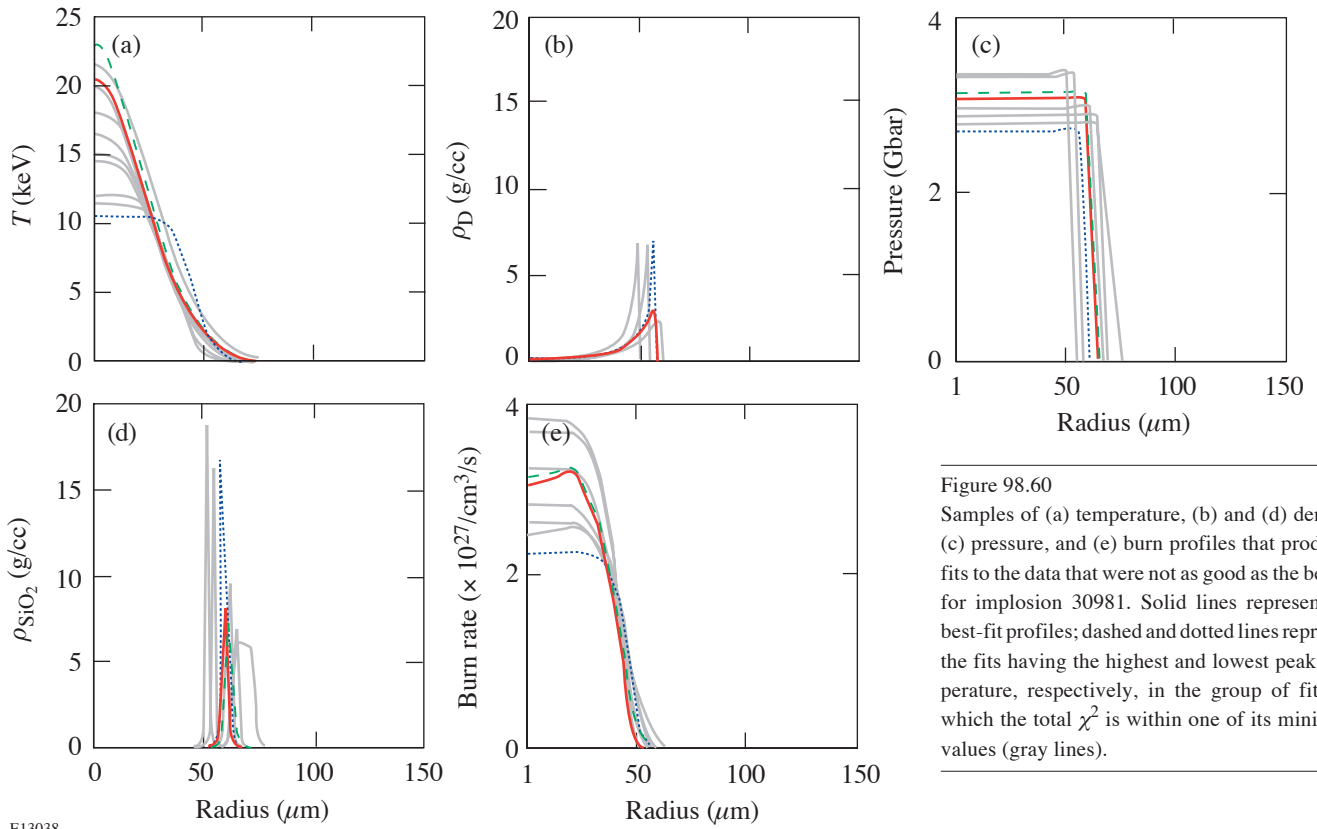


Figure 98.60  
 Samples of (a) temperature, (b) and (d) density, (c) pressure, and (e) burn profiles that produced fits to the data that were not as good as the best fit for implosion 30981. Solid lines represent the best-fit profiles; dashed and dotted lines represent the fits having the highest and lowest peak temperature, respectively, in the group of fits for which the total  $\chi^2$  is within one of its minimum values (gray lines).

E13038

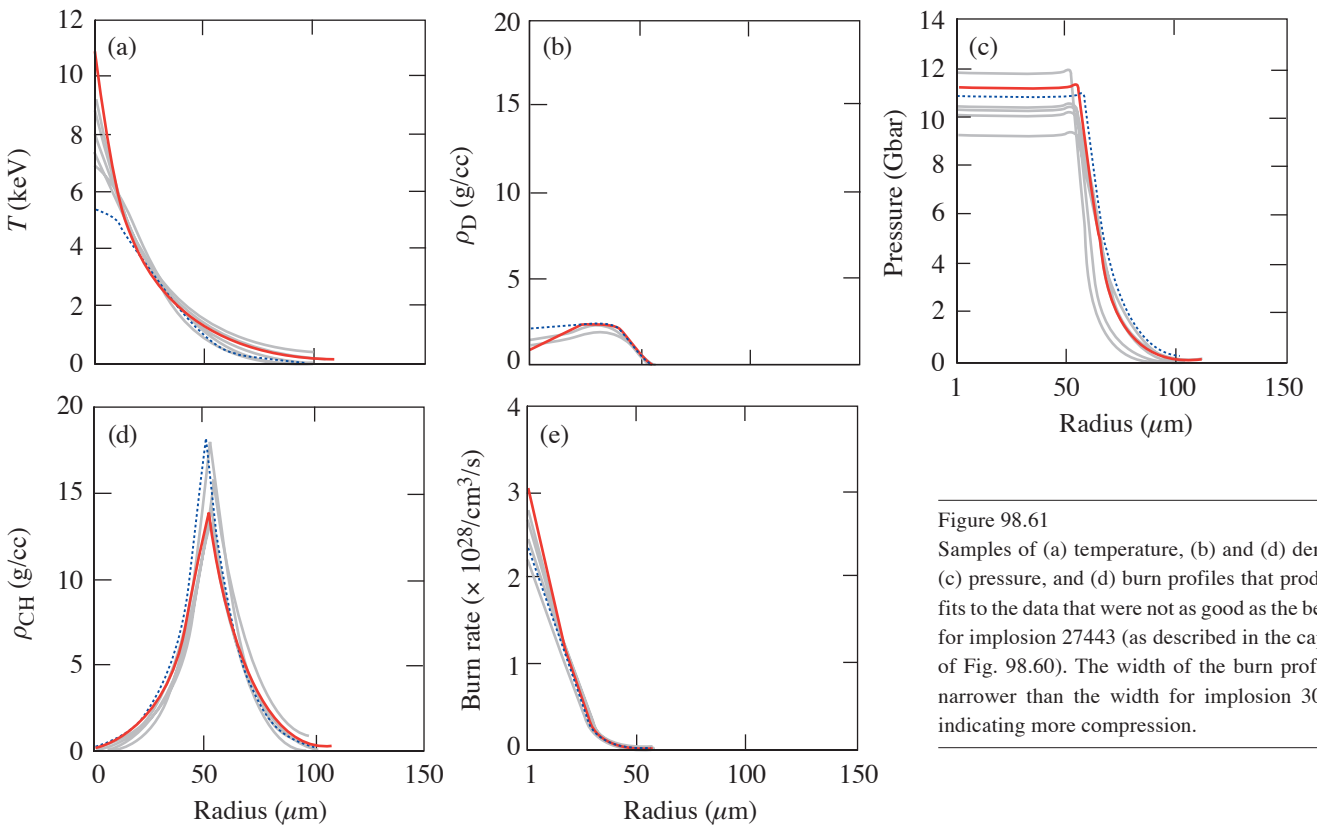
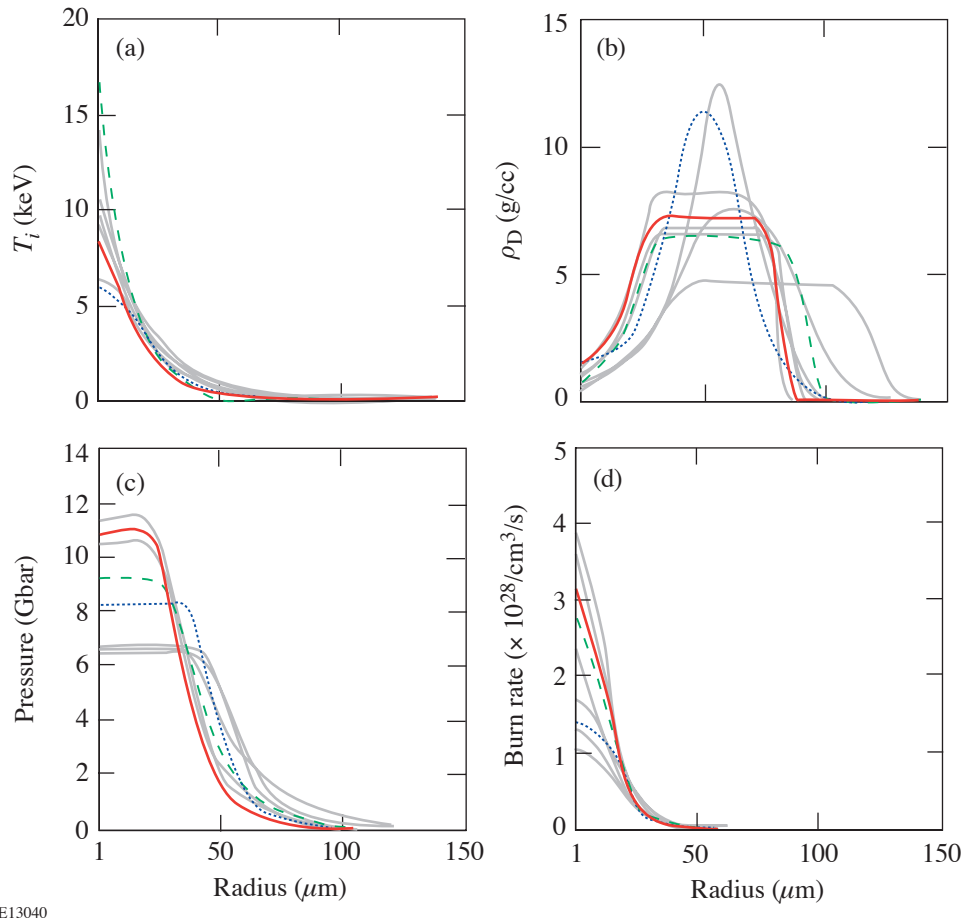


Figure 98.61  
 Samples of (a) temperature, (b) and (d) density, (c) pressure, and (d) burn profiles that produced fits to the data that were not as good as the best fit for implosion 27443 (as described in the caption of Fig. 98.60). The width of the burn profile is narrower than the width for implosion 30981, indicating more compression.

E13039



E13040

Figure 98.62

Samples of (a) temperature, (b) density, (c) pressure, and (d) burn profiles that produced fits to the data that were not as good as the best fit for implosion 28900 (as described in the caption of Fig. 98.60). The width of the burn profile is narrower than the width for implosion 30981, indicating more compression.

## ACKNOWLEDGMENT

The work was performed in part at LLE's National Laser Users' Facility (NLUF) and was supported in part by the U.S. DOE (grant DE-FG03-03SF22691), US DOE DP/NNSA (Cooperative Agreement DE-FG03-03NA00058), LLE (subcontract 412160-001G), and LLNL (subcontract B504974).

## REFERENCES

1. S. W. Haan *et al.*, Phys. Plasmas **2**, 2480 (1995).
2. J. D. Lindl, R. L. McCrory, and E. M. Campbell, Phys. Today **45**, 32 (1992).
3. J. D. Lindl, Phys. Plasmas **2**, 3933 (1995).
4. H. D. Campbell and F. H. Southworth, in *1st Topical Meeting on the Technology of Controlled Nuclear Fusion* (American Nuclear Society, Hinsdale, IL, 1974), pp. 75–76.
5. E. G. Gamalii *et al.*, JETP Lett. **21**, 70 (1975).
6. S. Skupsky and S. Kacenjar, J. Appl. Phys. **52**, 2608 (1981).
7. T. E. Blue and D. B. Harris, Nucl. Sci. Eng. **77**, 463 (1981).
8. T. E. Blue *et al.*, J. Appl. Phys. **54**, 615 (1983).
9. H. Azechi, M. D. Cable, and R. O. Stapf, Laser Part. Beams **9**, 119 (1991).
10. M. D. Cable and S. P. Hatchett, J. Appl. Phys. **62**, 2233 (1987).
11. H. Azechi *et al.*, Appl. Phys. Lett. **49**, 555 (1986).
12. F. H. Séguin, C. K. Li, D. G. Hicks, J. A. Frenje, K. M. Green, R. D. Petrasso, J. M. Soures, D. D. Meyerhofer, V. Yu. Glebov, C. Stoeckl, P. B. Radha, S. Roberts, C. Sorce, T. C. Sangster, M. D. Cable, S. Padalino, and K. Fletcher, Phys. Plasmas **9**, 2725 (2002).
13. P. Amendt, R. E. Turner, and O. L. Landen, Phys. Rev. Lett. **89**, 165001 (2002).
14. T. C. Sangster, J. A. Delettrez, R. Epstein, V. Yu. Glebov, V. N. Goncharov, D. R. Harding, J. P. Knauer, R. L. Keck, J. D. Kilkenny, S. J. Loucks, L. D. Lund, R. L. McCrory, P. W. McKenty, F. J. Marshall, D. D. Meyerhofer, S. F. B. Morse, S. P. Regan, P. B. Radha, S. Roberts, W. Seka, S. Skupsky, V. A. Smalyuk, C. Sorce, J. M. Soures, C. Stoeckl, K. Thorp, J. A. Frenje, C. K. Li, R. D. Petrasso, F. H. Séguin, K. A. Fletcher, S. Padalino, C. Freeman, N. Izumi, J. A. Koch, R. A. Lerche, M. J. Moran, T. W. Phillips, and G. J. Schmid, Phys. Plasmas **10**, 1937 (2003).
15. C. Stoeckl, C. Chiritescu, J. A. Delettrez, R. Epstein, V. Yu. Glebov, D. R. Harding, R. L. Keck, S. J. Loucks, L. D. Lund, R. L. McCrory, P. W. McKenty, F. J. Marshall, D. D. Meyerhofer, S. F. B. Morse, S. P. Regan, P. B. Radha, S. Roberts, T. C. Sangster, W. Seka, S. Skupsky, V. A. Smalyuk, C. Sorce, J. M. Soures, R. P. J. Town, J. A. Frenje, C. K. Li, R. D. Petrasso, F. H. Séguin, K. Fletcher, S. Padalino, C. Freeman, N. Izumi, R. Lerche, and T. W. Phillips, Phys. Plasmas **9**, 2195 (2002).
16. R. E. Turner, P. A. Amendt, O. L. Landen, L. J. Suter, R. J. Wallace, H. E. Dalhed, B. A. Hammel, and V. Glebov, Bull. Am. Phys. Soc. **47**, 328 (2002).
17. T. R. Boehly, D. L. Brown, R. S. Craxton, R. L. Keck, J. P. Knauer, J. H. Kelly, T. J. Kessler, S. A. Kumpan, S. J. Loucks, S. A. Letzring, F. J. Marshall, R. L. McCrory, S. F. B. Morse, W. Seka, J. M. Soures, and C. P. Verdon, Opt. Commun. **133**, 495 (1997).
18. S. Glasstone and R. H. Lovberg, *Controlled Thermonuclear Reactions: An Introduction to Theory and Experiment* (Van Nostrand, Princeton, NJ, 1960).
19. C. K. Li and R. D. Petrasso, Phys. Rev. Lett. **70**, 3059 (1993).
20. P. B. Radha, J. Delettrez, R. Epstein, V. Yu. Glebov, R. Keck, R. L. McCrory, P. McKenty, D. D. Meyerhofer, F. Marshall, S. P. Regan, S. Roberts, T. C. Sangster, W. Seka, S. Skupsky, V. Smalyuk, C. Sorce, C. Stoeckl, J. Soures, R. P. J. Town, B. Yaakobi, J. Frenje, C. K. Li, R. Petrasso, F. Séguin, K. Fletcher, S. Padalino, C. Freeman, N. Izumi, R. Lerche, and T. W. Phillips, Phys. Plasmas **9**, 2208 (2002).
21. C. K. Li, F. H. Séguin, J. A. Frenje, S. Kurebayashi, R. D. Petrasso, D. D. Meyerhofer, J. M. Soures, J. A. Delettrez, V. Yu. Glebov, P. B. Radha, F. J. Marshall, S. P. Regan, S. Roberts, T. C. Sangster, and C. Stoeckl, Phys. Rev. Lett. **89**, 165002 (2002).
22. S. P. Regan, J. A. Delettrez, F. J. Marshall, J. M. Soures, V. A. Smalyuk, B. Yaakobi, V. Yu. Glebov, P. A. Jaanimagi, D. D. Meyerhofer, P. B. Radha, W. Seka, S. Skupsky, C. Stoeckl, R. P. J. Town, D. A. Haynes, Jr., I. E. Golovkin, C. F. Hooper, Jr., J. A. Frenje, C. K. Li, R. D. Petrasso, and F. H. Séguin, Phys. Rev. Lett. **89**, 085003 (2002).
23. Y. Lin, T. J. Kessler, and G. N. Lawrence, Opt. Lett. **20**, 764 (1995).
24. T. R. Boehly, V. A. Smalyuk, D. D. Meyerhofer, J. P. Knauer, D. K. Bradley, R. S. Craxton, M. J. Guardalben, S. Skupsky, and T. J. Kessler, J. Appl. Phys. **85**, 3444 (1999).
25. S. Skupsky, R. W. Short, T. Kessler, R. S. Craxton, S. Letzring, and J. M. Soures, J. Appl. Phys. **66**, 3456 (1989).
26. Short laser pulses (<1 ns) imploding thin-glass-shell capsules prevent significant nuclear production while the laser is on. This is important if  $\rho R_{\text{total}}$  is to be studied because the capsule can be charged to a significant potential relative to the target chamber wall due to laser-plasma interactions. The potential can cause an upshift of measured proton energies,<sup>35,38,39</sup> making it difficult to determine how much energy the protons lost while leaving the capsule (necessary for calculating  $\rho R_{\text{total}}$ ). The potential decays away rapidly after the laser is turned off, so it does not affect measurements of protons from implosions in which the nuclear burn occurs after the pulse (such as those involving thick-plastic-shell or cryogenic capsules<sup>35</sup>). This affects only the study of  $\rho R_{\text{total}}$ ; measurements of yields are unaffected by capsule potentials.
27. F. H. Séguin, J. A. Frenje, C. K. Li, D. G. Hicks, S. Kurebayashi, J. R. Rygg, B.-E. Schwartz, R. D. Petrasso, S. Roberts, J. M. Soures, D. D. Meyerhofer, T. C. Sangster, J. P. Knauer, C. Sorce, V. Yu. Glebov, C. Stoeckl, T. W. Phillips, R. J. Leeper, K. Fletcher, and S. Padalino, Rev. Sci. Instrum. **74**, 975 (2003).

28. M. A. Russotto and R. L. Kremens, *Rev. Sci. Instrum.* **61**, 3125 (1990).
29. R. A. Lerche, D. W. Phillion, and G. L. Tietbohl, *Rev. Sci. Instrum.* **66**, 933 (1995).
30. V. Yu. Glebov, C. Stoeckl, S. Roberts, T. C. Sangster, J. A. Frenje, R. D. Petrasso, R. A. Lerche, and R. L. Griffith, *Bull. Am. Phys. Soc.* **48**, 342 (2003).
31. Primary-neutron-yield-weighted average ion temperature is calculated by two methods, each yielding a virtually identical temperature. First, the product of the temperature and the primary neutron birth rate per unit length at each radius is integrated and divided by the primary neutron yield. Second, the primary neutron spectrum is calculated, and the width of the spectrum is used to obtain an ion temperature.
32. J. D. Lindl, *Inertial Confinement Fusion: The Quest for Ignition and Energy Gain Using Indirect Drive* (Springer-Verlag, New York, 1998).
33. M. D. Rosen and J. H. Nuckolls, *Phys. Fluids* **22**, 1393 (1979).
34. M. J. Canavan, MIT, private communication (2004); herein the laser energy was  $\sim 30$  kJ for these DT implosions.
35. C. K. Li, F. H. Séguin, D. G. Hicks, J. A. Frenje, K. M. Green, S. Kurebayashi, R. D. Petrasso, D. D. Meyerhofer, J. M. Soures, V. Yu. Glebov, R. L. Keck, P. B. Radha, S. Roberts, W. Seka, S. Skupsky, C. Stoeckl, and T. C. Sangster, *Phys. Plasmas* **8**, 4902 (2001).
36. P. B. Radha *et al.*,<sup>20</sup> C. K. Li *et al.*,<sup>21</sup> and S. P. Regan *et al.*<sup>22</sup> reported  $\sim 1 \mu\text{m}$ ,  $\sim 0.5 \mu\text{m}$ , and  $\sim 0.4 \mu\text{m}$  of the initial shell layer mixed into the fuel, respectively.
37. V. A. Smalyuk, J. A. Delettrez, S. B. Dumanis, R. Epstein, V. Yu. Glebov, D. D. Meyerhofer, P. B. Radha, T. C. Sangster, C. Stoeckl, N. C. Toscano, J. A. Frenje, C. K. Li, R. D. Petrasso, F. H. Séguin, and J. H. Koch, "Hot-Core Characterization of the Cryogenic  $D_2$  Target at Peak Neutron Production in Direct-Drive Spherical Implosion," submitted to *Physical Review Letters*.
38. D. G. Hicks, C. K. Li, F. H. Séguin, J. D. Schnittman, A. K. Ram, J. A. Frenje, R. D. Petrasso, J. M. Soures, D. D. Meyerhofer, S. Roberts, C. Sorce, C. Stoeckl, T. C. Sangster, and T. W. Phillips, *Phys. Plasmas* **8**, 606 (2001).
39. D. G. Hicks, C. K. Li, F. H. Séguin, A. K. Ram, J. A. Frenje, R. D. Petrasso, J. M. Soures, V. Yu. Glebov, D. D. Meyerhofer, S. Roberts, C. Sorce, C. Stöckl, T. C. Sangster, and T. W. Phillips, *Phys. Plasmas* **7**, 5106 (2000).